International Tables for Crystallography (2018). Vol. H, Section 3.1.2, pp. 224–230.

3.1. The optics and alignment of the divergent-beam laboratory X-ray powder diffractometer and its calibration using NIST standard reference materials

J. P. Cline, M. H. Mendenhall, D. Black, D. Windover and A. Henins

3.1.1. Introduction

The laboratory X-ray powder diffractometer has several virtues that have made it a principal characterization device for providing critical data for a range of technical disciplines involving crystalline materials. The specimen is typically composed of small crystallites (5–30 μm), which is a form that is suitable for a wide variety of materials. A continuous set of reflections can be collected with a single scan in θ–2θ angle space. Not only can timely qualitative analyses be carried out, but with the more advanced data-analysis methods a wealth of quantitative information may be extracted. Modern commercial instruments may include features that include focusing mirror optics and the ability to change quickly between various experimental configurations. In this chapter, we discuss results from a NIST-built diffractometer with features specific to the collection of data that complement the NIST effort in standard reference materials (SRMs) for powder diffraction. While this machine can be configured with focusing optics, here we consider only those configurations that use a divergent beam in Bragg–Brentano, para-focusing geometry.

A principal advantage of the divergent-beam X-ray powder diffractometer is that a relatively large number of crystallites are illuminated, providing a strong diffraction signal from a representative portion of the sample. However, the para-focusing optics of laboratory diffractometers produce patterns that display profiles of a very complex shape. The observed 2θ position of maximum diffraction intensity does not necessarily reflect the true spacing of the lattice planes (*hkl*). While advanced data-analysis methods can be used to model the various aberrations and account for the observed profile shape and position, there are a number of instrumental effects for which there is not enough information for reliable, *a priori* modelling of the performance of the instrument. The task may be further compounded when instruments are set up incorrectly, because the resultant additional errors are convoluted into the already complex set of aberrations. Therefore, the results are often confounding, as the origin of the difficulty is problematic to discern. The preferred method for avoiding these situations is the use of SRMs to calibrate the instrument performance. We will describe the various methods with which NIST SRMs may be used to determine sources of measurement error, as well as the procedures that can be used to properly calibrate the laboratory X-ray powder diffraction (XRPD) instrument.

The software discussed throughout this manuscript will include commercial as well as public-domain programs, some of which were used for the certification of NIST SRMs. In addition to the NIST disclaimer concerning the use of commercially available resources,[1] we emphasize that some of the software presented here was also developed to a certain extent through longstanding collaborative relationships between the first author and the respective developers of the codes. The codes that will be discussed include: *GSAS* (Larson & Von Dreele, 2004), the PANalytical software *HighScore Plus* (Degen *et al.*, 2014), the Bruker codes *TOPAS* (version 4.2) (Bruker AXS, 2014) and *DIFFRAC.EVA* (version 3), and the Rigaku code *PDXL 2* (version 2.2) (Rigaku, 2014). The fundamental-parameters approach (FPA; Cheary & Coelho, 1992) for modelling X-ray powder diffraction line profiles, as implemented in *TOPAS*, has been used since the late 1990s for the certification of NIST SRMs. To examine the efficacy of the FPA models, as well as their implementation in *TOPAS*, we have developed a Python-based code, the NIST Fundamental Parameters Approach Python Code (*FPAPC*), that replicates the FPA method in the computation of X-ray powder diffraction line profiles (Mendenhall *et al.*, 2015). This FPA capability is to be incorporated into *GSASII* (Toby & Von Dreele, 2013).

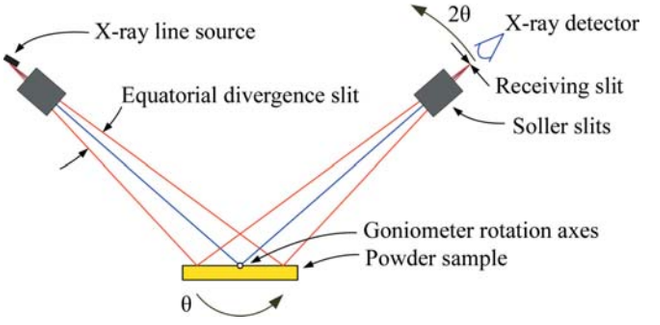

Figure 3.1.1
A schematic diagram illustrating the operation and optical components of a Bragg–Brentano X-ray powder diffractometer.

3.1.2. The instrument profile function

The instrument profile function (IPF) describes the profile shape and displacement as a function of 2θ that is the intrinsic instrumental response imparted to any data collected with that specific instrument. It is a function of the radiation used, the instrument geometry and configuration, slit sizes *etc*.[2] The basic optical layout of a divergent-beam X-ray powder diffractometer of Bragg–Brentano, para-focusing geometry using a tube anode in a line-source configuration is illustrated in Fig. 3.1.1. This figure shows the various optical components in the plane of diffraction, or equatorial plane. The dimensions of the optical components shown in Fig. 3.1.1 and the dimensions of the goniometer itself determine the resolution of the diffractometer. The divergent nature of the X-ray beam will increase the number of crystallites giving rise to the diffraction signal; the incident-beam slit defines an angular range within which crystallites will be oriented such that their diffraction is registered. One of the manifestations of this geometry is that knowledge of both the diffraction angle and

[1] Certain commercial equipment, instruments, or materials are identified in this in order to adequately specify the experimental procedure. Such identification does not imply recommendation or endorsement by the National Institute of Standards and Technology, nor does it imply that the materials or equipment identified are necessarily the best available for the purpose.

[2] See Chapters 3.6 and 5.1 for details of contributions to the profile shape from the sample.

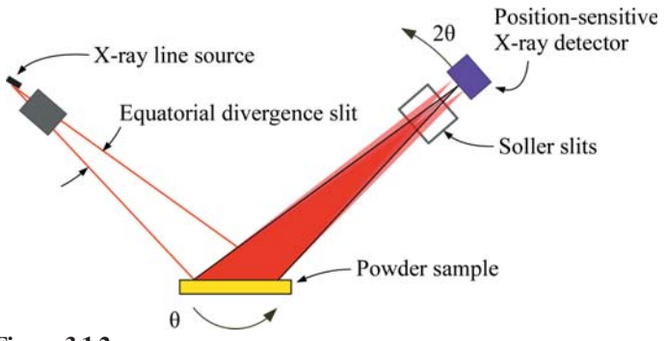

Figure 3.1.2
A schematic diagram illustrating the operation and optical components of a Bragg–Brentano X-ray diffractometer equipped with a position-sensitive detector. Only the rays striking the centre line of the PSD, outlined in black, are in accordance with Bragg–Brentano focusing.

specimen position are critical for the correct interpretation of the data. The goniometer radius is the distance between the rotation axes and the X-ray source (R_1), or the distance between the rotation axes and receiving slit (R_2), as shown in Fig. 3.1.1; these two distances must be equal. The specimen surface is presumed to be on the rotation axes; however, this condition is rarely realized and it is common to have to consider a specimen-displacement error.

Goniometer assemblies themselves can be set up in several configurations. Invariably, two rotation stages are utilized. Fig. 3.1.1 illustrates a machine of $\theta/2\theta$ geometry: the tube is stationary while one stage rotates the specimen through angle θ, sometimes referred to as the angle Ω, while a second stage rotates the detector through angle 2θ. Another popular configuration is θ/θ geometry, where the specimen remains stationary and both the tube and detector rotate through angle θ. However, the diffraction optics themselves do not vary with regard to how the goniometer is set up.

The detector illustrated in Fig. 3.1.1 simply reads any photons arriving at its entrance window as the diffracted signal is analysed by the receiving slit. Such detectors, which often use a scintillation crystal, are typically referred to as point detectors. A diffracted-beam post-sample monochromator is often added to the beam path after the receiving slit to filter out any fluorescence from the sample. The crystal optic of these monochromators typically consists of pyrolytic graphite with a high level of mosaicity that is bent to a radius in rough correspondence to that of the goniometer. This imposes a relatively broad energy bandpass of approximately 200 eV (with 8 keV Cu $K\alpha$ radiation) in width on the diffracted beam. This window is centred so as to straddle that of the energy of the source radiation being used, thereby filtering fluorescent and other spurious radiation from the detector while transmitting the primary features of the emission spectrum, presumably without distortion.

Within the last decade, however, the popularity of this geometry has fallen markedly, as the use of the post-sample monochromator/point-detector assembly has been largely displaced by the use of a position-sensitive detector (PSD). This geometry is illustrated in Fig. 3.1.2. A line detector replaces the point detector, and offers the ability to discriminate with respect to the position of arriving X-rays within the entrance window of the PSD. A multichannel analyser is typically used to map the arriving photons from the PSD window into 2θ space. Depending on the size of the PSD entrance window, increases in the counting rate by two orders of magnitude relative to a point detector can be easily achieved. Furthermore, this is accomplished by including the signal from additional crystallites, mitigating any problems with particle-counting statistics (Fig. 3.1.2). A drawback to the PSD is that the increased intensity is achieved with the inclusion of signals that are not within the Bragg–Brentano focusing regimen (compare Figs. 3.1.1 and 3.1.2), leading to a broadening of the line profiles. The level of broadening is proportional to the size of the PSD entrance window and inversely proportional to 2θ angle. The move to PSDs has been further augmented by the development of solid-state, silicon strip detectors that offer the advantages of a PSD without the maintenance issues of the early gas-flow proportional PSDs. Fluorescence can be problematic with a PSD; however, the problem can be countered with the use of filters. More recent developments in electronics have improved the ability of these PSDs to discriminate with respect to energy. We discuss only this newer class of solid-state linear PSDs in this chapter.

A monochromator can also be used to condition the incident beam so that it will consist exclusively of $K\alpha_1$ radiation. Monochromators of this nature are inserted into the beam path prior to the beam's arrival at the incident-beam slit shown in Fig. 3.1.1. These devices typically use a Ge(111) crystal as the optic; Ge monochromators have a much smaller energy bandpass than graphite monochromators. They are, therefore, much more complex and difficult to align. Here we discuss an incident-beam monochromator (IBM) using a Johansson focusing optic (Johansson, 1933), as shown in Fig. 3.1.3. When incorporating an IBM assembly into a powder diffractometer using reflection geometry, the focal line of the optic must be positioned on the goniometer radius as per the line source of the tube anode in a conventional setup, shown in the right-hand

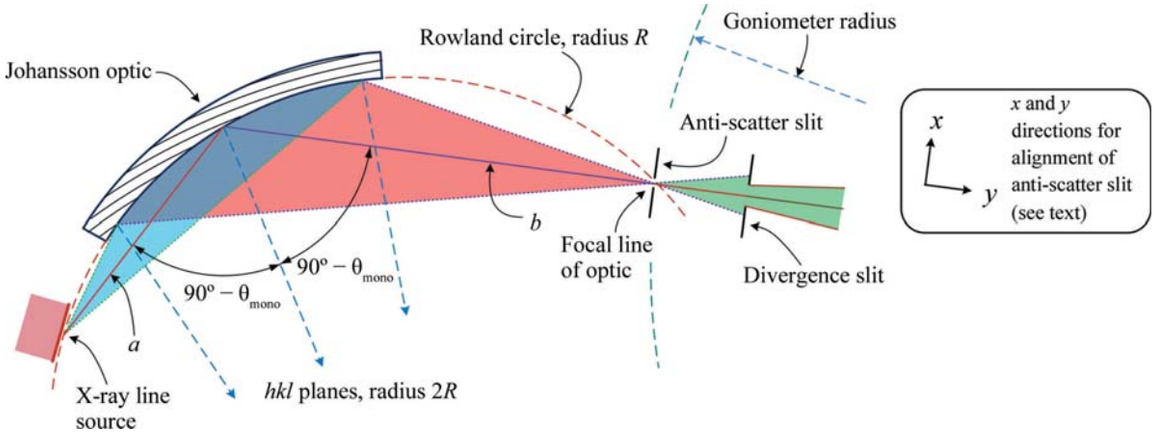

Figure 3.1.3
A schematic diagram illustrating the geometry of a Johansson incident-beam monochromator.

Table 3.1.1
Aberrations comprising the geometric component of the IPF

Aberration	Controlling parameters	Impact
X-ray source width (w_x)	Angle subtended by source: w_x/R	Symmetric broadening
Receiving-slit width or PSD strip width (w_r)	Angle subtended by slit/strip: w_r/R	Symmetric broadening
Flat specimen error/equatorial divergence	Angle of divergence slit: α	Asymmetric broadening to low 2θ, with decreasing 2θ
PSD defocusing	PSD window width, angle of divergence slit: α	Symmetric broadening with $1/(\tan\theta)$
Axial divergence Case 1: no Soller slits Case 2: Soller slits define divergence angle	 Axial lengths of the X-ray source (L_x), sample (L_s) and receiving slit (L_r) relative to goniometer radius (R) Acceptance angles Δ_I and Δ_D of the incident- and diffracted-beam Soller slits	Below $\sim 100°$: asymmetric broadening to low 2θ, with decreasing 2θ else to high 2θ, with increasing 2θ
Specimen transparency	Penetration factor relative to diffractometer radius $1/\mu R$	Asymmetric broadening to low 2θ, with $\sin(2\theta)$
Specimen displacement z height	Displacement of specimen surface from goniometer rotation axes	Displacement of profiles with $\cos\theta$

side of Fig. 3.1.3. In this way, a Johansson optic provides a monochromatic X-ray source, passing some portion of the $K\alpha_1$ emission spectrum, while preserving the divergent-beam Bragg–Brentano geometry as shown in Figs. 3.1.1 and 3.1.2. The use of an IBM reduces the number of spectral contributions to the observed line shape and results in an IPF that is more readily modelled with conventional profile fitting. Furthermore, equipping such a machine with a PSD affords all of its advantages, while the elimination of the *Bremsstrahlung* by the IBM reduces the impact of fluorescence that can otherwise be problematic with a PSD.

Throughout this manuscript we use the terms 'width' and 'length' when referring to the optics. Width expresses extent in the equatorial plane. Length is used to denote a physical dimension parallel to the rotation axes of the goniometer as defined in Fig. 3.1.1. The designation of the axial divergence angle, as well as the specifications concerning Soller slits, will be considered in terms of the double angle, both for incoming and outgoing X-rays. This is in contrast to the generally accepted single-angle definition shown in Klug & Alexander (1974); hence the axial-divergence angles reported throughout this chapter are twice those that are often encountered elsewhere.

The observed line shape in powder diffraction consists of a convolution of contributions from the instrument optics (referred to as the geometric profile), the emission spectrum and the specimen, as shown diagrammatically for divergent-beam XRPD in Fig. 3.1.4. The specimen contribution is often the dominant one in a given experiment; however, we do not consider it to any great extent in this discussion. The factors comprising the geometric profile are listed in Table 3.1.1. Technically, neither of the last two items (specimen transparency and displacement) are components of the geometric profile of the instrument. They are functions of the specimen and the manner in which it was mounted. However, it is not possible to use a whole-pattern data-analysis method without considering these two factors; as they play a critical role in the modelling of the observed profile positions and shapes they are included in this discussion. The convolution of the components of the geometric profile and emission spectrum forms the IPF. As will be discussed, both of these contributions are complex in nature, leading to the well known difficulty in modelling the IPF from Bragg–Brentano equipment. This complexity, and the relatively limited q-space (momentum space) range accessible with laboratory equipment, tends to drive the structure solution and refinement community, with their expertise in the development of data-analysis procedures, towards the use of synchrotron and neutron sources. A significant number of the models and analytical functions discussed here were developed for, and are better suited to, powder-diffraction equipment using such nonconventional sources.

We now consider the geometric profile with an examination of the aberrations listed in Table 3.1.1. Figs. 3.1.5–3.1.10 illustrate simulations of the aberration function associated with the factors listed in Table 3.1.1. The first two of these, the source and receiving-slit width or silicon strip width with a PSD, simply cause symmetric broadening, constant with 2θ angle, and are typically described with 'impulse' or 'top-hat' functions. The flat specimen error is due to defocusing in the equatorial plane. One can see from Fig. 3.1.1 that for any beam that is not on the centre line of the goniometer, R_1 is not equal to R_2. The magnitude of the effect is directly

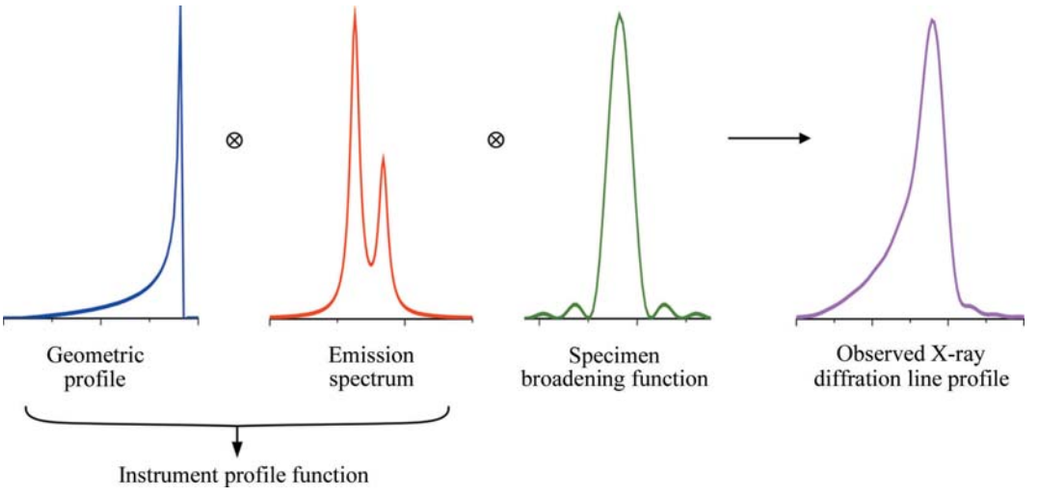

Figure 3.1.4
Diagrammatic representations of convolutions leading to the observed XRPD profile.

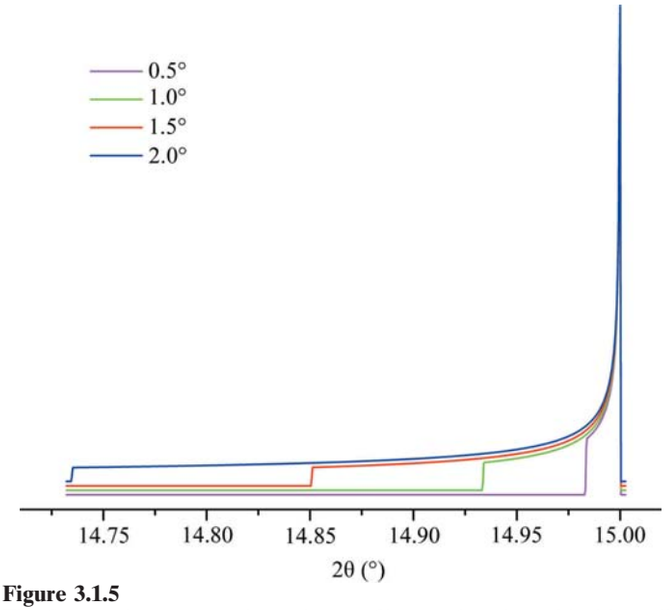

Figure 3.1.5
The flat specimen error aberration profile as a function of incident-slit size (R = 217.5 mm).

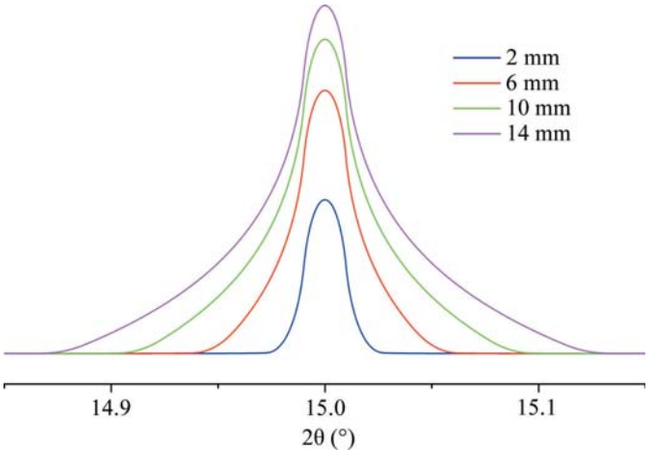

Figure 3.1.7
The PSD defocusing error aberration profiles for a silicon strip PSD as a function of window width (R = 217.5 mm, incident slit = 1° and strip width = 75 μm).

proportional to the divergent slit size as shown in Fig. 3.1.5. Its functional dependence on 2θ angle, *i.e.* 1/tan θ, is illustrated in Fig. 3.1.6. The flat specimen error leads to asymmetric profile broadening on the low-angle side, accentuated at decreasing values of 2θ. The functional dependence of this aberration on 2θ, shown in Fig. 3.1.6, is for a fixed slit; the use of a variable-divergence incident-beam slit to obtain a constant area of illumination reduces this dependence on the 2θ angle.

The broadening imparted to diffraction line profiles from the early gas-flow proportional PSDs was due to defocusing originating from both the equatorial width of the PSD window and parallax within the gas-filled counting chamber. Early models for these effects (Cheary & Coelho, 1994) included two parameters: one for the window width and a second for the parallax. The modern silicon strip PSDs do not need this second term as there is effectively no parallax effect. The aberration profile imparted to the data from a modern PSD (Mendenhall *et al.*, 2015) is illustrated in Fig. 3.1.7 as a function of window width. The profiles are symmetric about the centre line, exhibiting both increasing intensity and breadth as the window width is increased. The profile consists of two components: a central peak with a width independent of 2θ, which is due to the pixel strip width of the detector, and wings which are due to the defocusing. The breadths of the wings shown in Fig. 3.1.7 vary in proportion to the incident slit size and as 1/tan θ, and therefore are largely unobservable at high 2θ angles.

Cheary & Coelho (1998*a*,*b*) have modelled axial divergence effects in the context of two geometric cases. Case 1 is the situation in which the axial divergence is limited solely by the width of the beam path as determined by the length of the tube filament, the receiving slit and the size of the sample. The aberration function in which these parameters are 12 mm, 15 mm and 15 mm, respectively, is illustrated in Fig. 3.1.8; the extent of broadening is nearly 1° in 2θ at a 2θ angle of 15°. The other plots of Fig. 3.1.8 refer to a 'case 2' situation where axial divergence is limited by the inclusion of Soller slits in the incident- and diffracted-beam paths. One also has to consider the impact of a including a graphite post-monochromator. This would increase

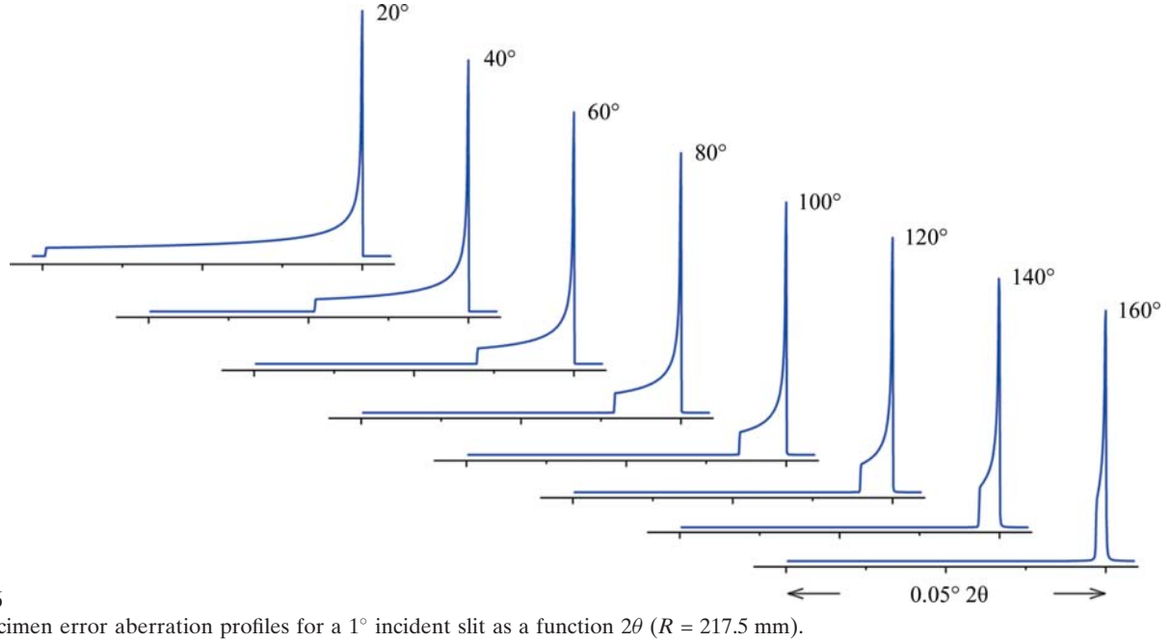

Figure 3.1.6
The flat specimen error aberration profiles for a 1° incident slit as a function 2θ (R = 217.5 mm).

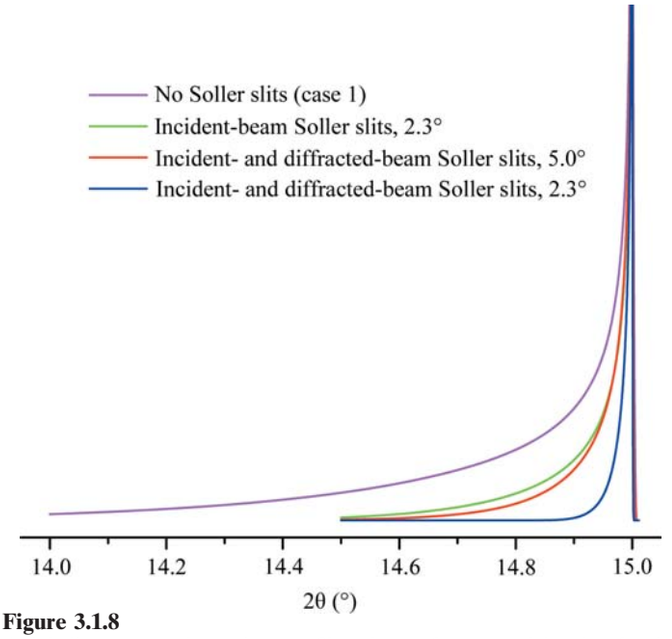

Figure 3.1.8
Axial divergence aberration profiles shown for several levels of axial divergence. Case 1 (of Table 3.1.1) is computed for a source length of 12 mm and a sample and receiving-slit length of 15 mm. The remaining three simulations include are of case 2, where Soller slits limit the axial divergence (R = 217.5 mm).

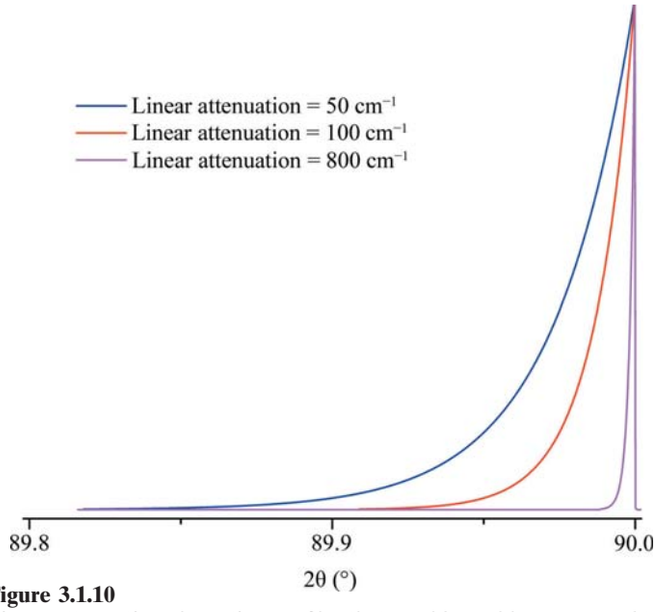

Figure 3.1.10
Linear attenuation aberration profiles that would roughly correspond to SRMs 676a (50 cm^{-1}), 640e and 1976b (100 cm^{-1}), and 660c (800 cm^{-1}) at 90° 2θ, where the transparency effect is at a maximum (R = 217.5 mm).

the path length of the diffracted beam by 10 to 15 cm, reducing axial divergence effects substantially and effectively functioning as a Soller slit. Cheary & Cline (1995) determined that the inclusion of a Soller slit with a post-monochromator did result in a slight improvement in resolution; however, this was at the cost of a threefold reduction in intensity. We do not use Soller slits in the diffracted beam when using a post-monochromator. The 5° primary and secondary Soller slit aberration profile of Fig. 3.1.8 corresponds to an instrument with a primary Soller slit and a graphite post-monochromator. The profiles shown for the two 2.3° Soller-slit configurations actually constitute a fairly high level of collimation given the double-angle definition of the specifications. Fig. 3.1.9 shows the functional dependence of the aberration profile for two 2.3° Soller slits on 2θ. Below approximately 100°, the effect increases with decreasing 2θ. Approximate symmetry is observed at 100°, while asymmetry to high angle increases thereafter. The aberration profile associated with specimen transparency to the X-ray beam is illustrated in Fig. 3.1.10. The figure shows the impact at 90° 2θ where the effect is at its maximum. The observed profile is broadened asymmetrically to low 2θ; the effect drops off in a largely symmetric manner with 2θ on either side of 90°.

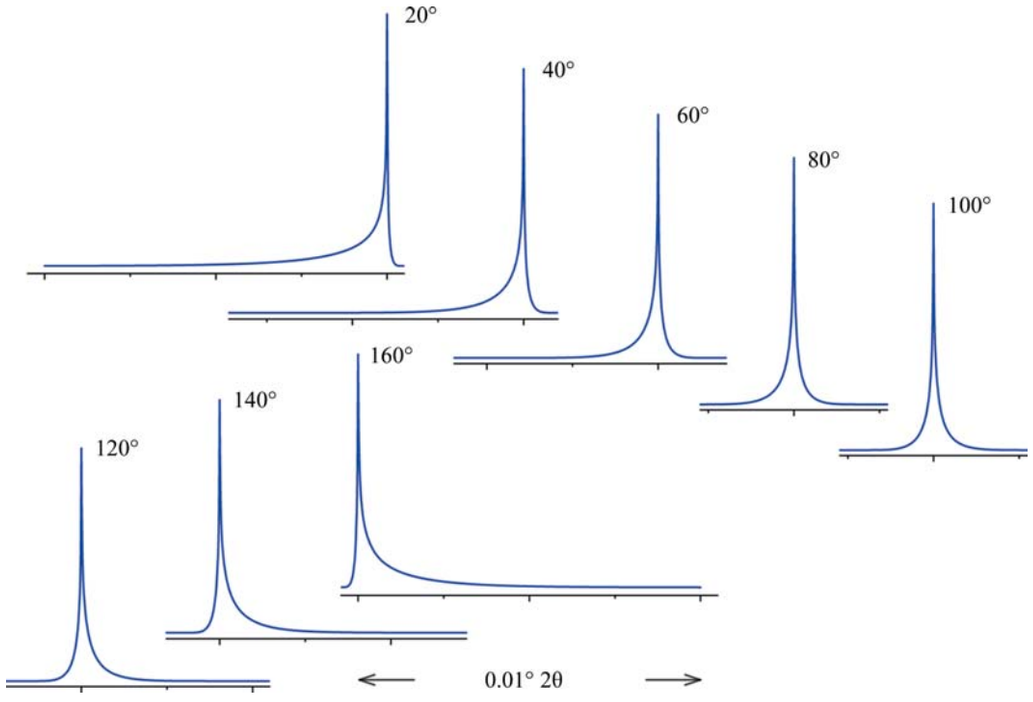

Figure 3.1.9
Axial divergence aberration profiles for primary and secondary Soller slits of 2.3° as a function of 2θ (R = 217.5 mm).

The wavelength profile or emission spectrum with its characterization on an absolute energy scale provides the traceability of the diffraction measurement to the International System of Units (SI) (BIPM, 2006). The currently accepted characterization of the emission spectrum of Cu $K\alpha$ radiation is provided by Hölzer *et al.* (1997) and is shown in Fig. 3.1.11. The spectrum is modelled with four Lorentzian profile shape functions (PSFs): two large ones for the primary $K\alpha_1$ and $K\alpha_2$ profiles, and two smaller ones displaced slightly to lower energy to account for the asymmetry in the observed line shape. The data shown in Fig. 3.1.11 are in energy space and are transformed into 2θ space with the dispersion relation. This is obtained by differentiating

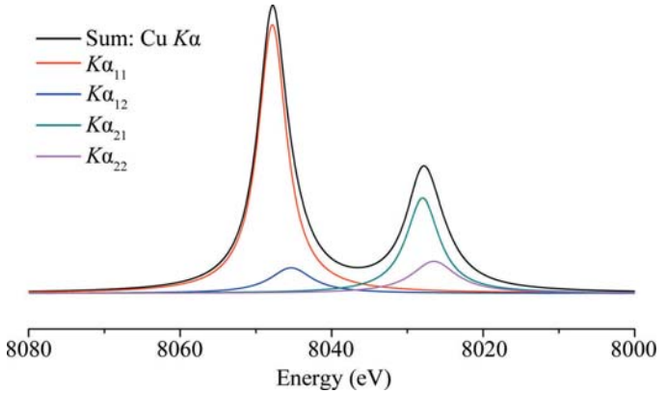

Figure 3.1.11
The emission spectrum of Cu $K\alpha$ radiation as provided by Hölzer *et al.* (1997), represented by four Lorentzian profiles: two primary ones and a pair of smaller ones to account for the observed asymmetry. The satellite lines, often referred to as the $K\alpha_3$ lines, are not displayed.

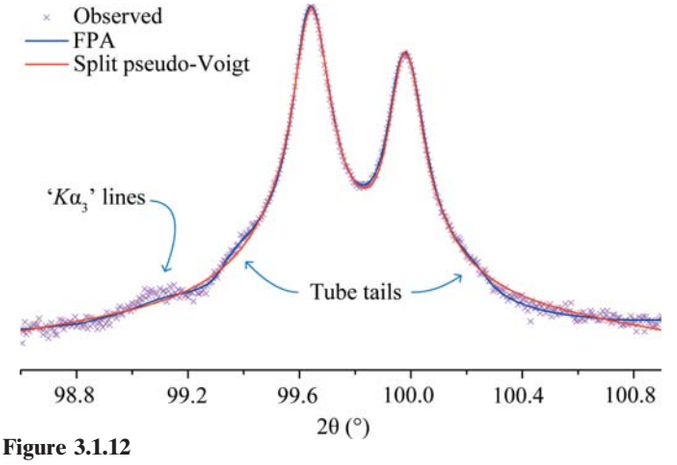

Figure 3.1.12
Illustration of the $K\alpha_3$ lines and tube-tails contributions to an observed profile on a log scale, shown with two fits: the fundamental-parameters approach, which includes these features, and the split pseudo-Voigt PSF, which does not.

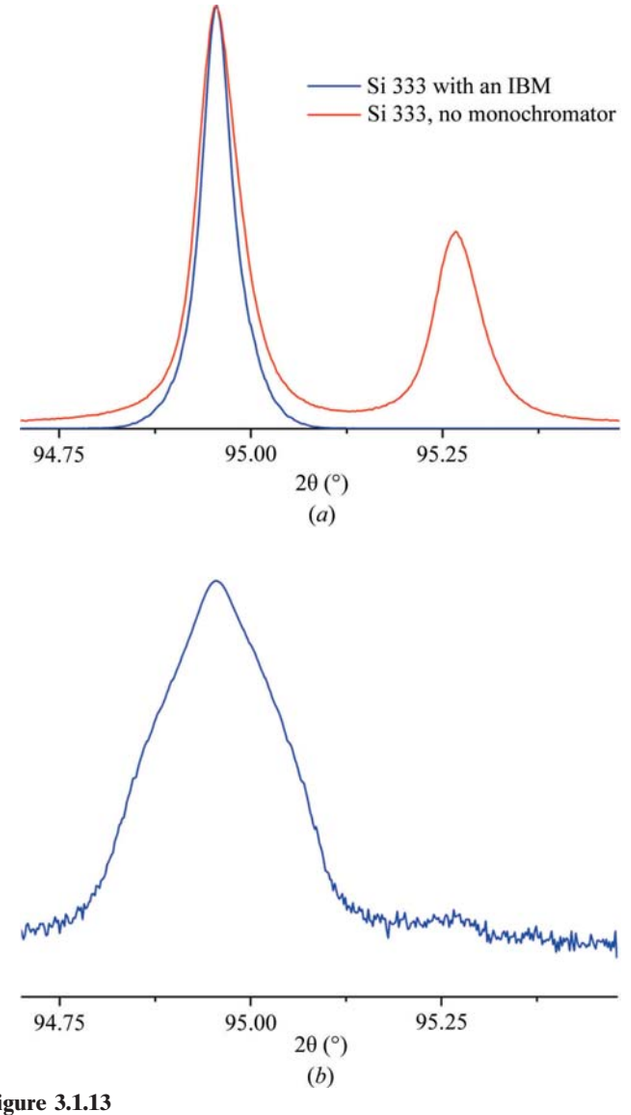

Figure 3.1.13
Illustration of the effect of the Johansson optic on the Cu $K\alpha$ emission spectrum. (*a*) Data collected for the Si 333 single-crystal reflection on a linear scale. (*b*) Analogous data from Johansson optic alone on a log scale. Both data sets were collected with 0.05 mm incident and receiving slits. The near absence of the $K\alpha_2$ scatter displayed in (*b*) can only be realized with the use of a properly aligned anti-scatter slit located at the focal line of the optic.

Bragg's law to obtain $d\theta/d\lambda$. The dominant term in the result is $\tan\theta$, which leads to the well known 'stretching' of the wavelength distribution with respect to 2θ. Maskil & Deutsch (1988) characterized a series of satellite lines in the Cu $K\alpha$ spectrum with an energy centred around 8080 eV and an intensity relative to the $K\alpha_1$ line of 6×10^{-3}. These are sometimes referred to as the $K\alpha_3$ lines, and are typically modelled with a single Lorentzian within the FPA. The 'tube tails' as reported by Bergmann *et al.* (2000) are a contribution that is strictly an artifact of how X-rays are produced in the vast majority of laboratory diffractometers. With the operation of an X-ray tube, off-axis electrons are also accelerated into the anode and produce X-rays that originate from positions other than the desired line source. They are not within the expected trajectory of para-focusing X-ray optics and produce tails on either side of a line profile as illustrated, along with the $K\alpha_3$ lines, in Fig. 3.1.12. Lastly, the energy bandpass of the pyrolytic graphite crystals used in post-monochromators is not a top-hat (or square-wave) function. Thus, the inclusion of a post-monochromator influences the observed emission spectrum.

A Johansson IBM dramatically reduces the complexity of the IPF by largely removing the $K\alpha_2$, $K\alpha_3$ and tube-tails contributions to the observed profile shape. The vast majority of the *Bremsstrahlung* is also removed. Furthermore, the inclusion of the IBM increases the path length of the incident beam by 25 to 30 cm. This substantially reduces the contribution of axial divergence to the observed profile shape. The crystals used are almost exclusively germanium (the 111 reflection), and are ground and bent to the Johansson focusing geometry, as shown in Fig. 3.1.3. They can be symmetric, with the source-to-crystal distance a and the crystal-to-focal point distance b being equal, in which case they will exhibit a bandpass of the order of 8 eV. They will slice a central portion out of the $K\alpha_1$ line, clipping the tails, to transmit perhaps 70% of the original width of the Cu $K\alpha_1$ emission spectrum. This yields a symmetric profile shape of relatively high resolution, or reduced profile breadth (other parameters being equal). The crystals can also be asymmetric, with the distance a being ~60% of the distance b. These optics will exhibit a bandpass of the order of 15 eV, in which case they transmit most of the $K\alpha_1$ line for a higher intensity, but with a lower resolution. The optic discussed here is of the latter geometry, as shown in Fig. 3.1.3.

A potential drawback to the use of an IBM concerns the nature of the $K\alpha_1$ emission spectrum it transmits, which may preclude the use of data-analysis methods that are based upon an accurate

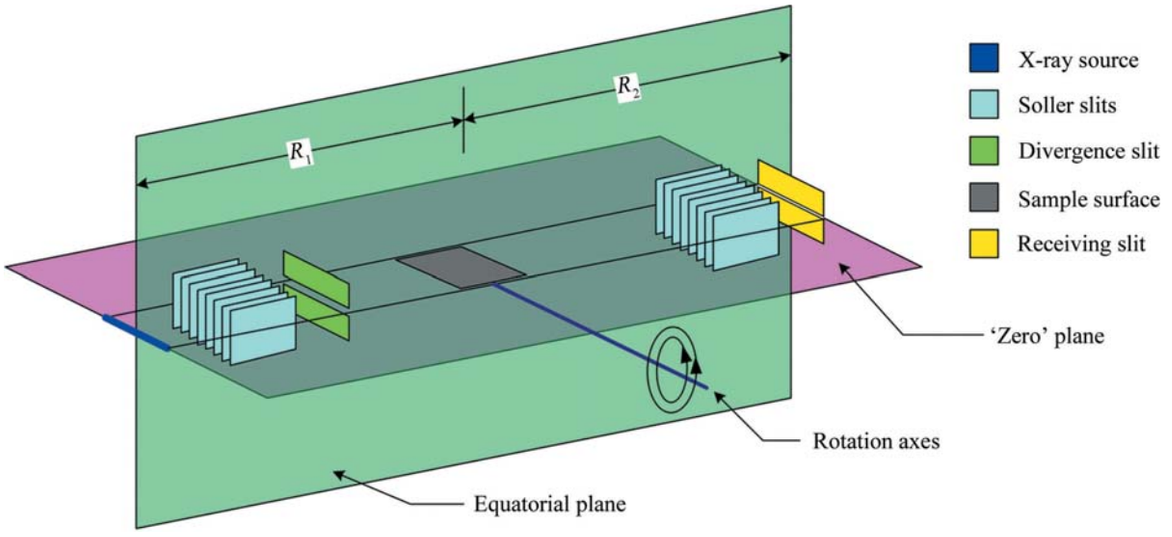

Figure 3.1.14
Diagrammatic explanation of the conditions necessary to realize a properly aligned X-ray powder diffractometer.

mathematical description of an incident spectrum. At best, a 'perfect' focusing crystal will impose an uncharacterized, though somewhat Gaussian, energy filter on the beam it diffracts. However, in certain optics the required bend radius of Johansson geometry is realized by clamping the crystal onto a curved form. The clamping restraint exists only at the edges of the optic, not in the central, active area where it is illuminated by the X-ray beam. The crystal itself however, can minimize internal stress by remaining flat; in this case an anticlastic curvature of the optic results. A 'saddle' distortion across the surface of the diffracting region of the crystal results in a complex asymmetric $K\alpha_1$ spectrum that defies accurate mathematical description. Johansson optics, however, can be bent by cementing the crystals into a preform, yielding an optic of superior perfection in curvature. Fig. 3.1.13 shows data collected from such an optic using an Si single crystal, 333 reflection, as an analyser. Parallel-beam conditions were approximated in this experiment with the use of very fine 0.05 mm incident and receiving slits. The observed symmetric emission profile of Fig. 3.1.13(a) can be modelled with a combination of several Gaussians. However, a Johansson optic will scatter 1–2% of high-energy radiation to a higher 2θ angle than the $K\alpha_1$ focal line of the optic. This unwanted scatter is dominated by, but not exclusive to, the $K\alpha_2$ spectrum. Louër (1992) indicated that it can be largely blocked with a knife edge aligned to just 'contact' the high-angle side of the optic's focal line. Alternatively, the NIST method is to use a slit aligned to straddle the focal line. Proper alignment of this anti-scatter slit is critical to achieving a good level of performance with the absence of '$K\alpha_2$' scatter, as illustrated in Fig. 3.1.13(b). As will be demonstrated, with use of any Johansson optic the elimination of the $K\alpha_2$ line is of substantial benefit in fitting the observed peaks with analytical profile-shape functions.

3.1.3. Instrument alignment

Modern instruments embody the drive towards interchangeable pre-aligned or self-aligning optics, which, in turn, has led to several approaches to obtaining proper alignment with minimum effort on the part of the user. We will not review these approaches, but instead we decribe here the methods used at NIST, which could be used to check the alignment of newer equipment. With the use of calibration methods that simply characterize the performance (which includes the errors) of the machine in an empirical manner and apply corrections, the quality of the instrument alignment may be surprisingly uncritical for a number of basic applications such as lattice-parameter refinement. However, with the use of the more advanced methods for characterization of the IPF that are based on the use of model functions, the proper alignment of the machine is critical. The models invariably include refineable parameter(s) that characterize the extent to which the given aberration affects the data; the correction is applied, and the results are therefore 'correct'. However, if the instrument is not aligned properly, the analysis attempts to model the errors due to misalignment as if they were an expected aberration. The corrections applied are therefore incorrect in degree and nature and an erroneous result is obtained.

The conditions for proper alignment of a Bragg–Brentano diffractometer (see Fig. 3.1.14) are:

(1) the goniometer radius, defined by the source-to-rotation-axes distance, R_1, equals that defined by the rotation-axes-to-receiving-slit distance, R_2 (to ± 0.25 mm);
(2) the X-ray line source, sample and receiving slit are centred in the equatorial plane of diffraction (to ± 0.25 mm);
(3) the goniometer rotation axes are co-axial and parallel (to ± 5 μm and <10 arc seconds);
(4) the X-ray line source, specimen surface, detector slit and goniometer rotation axes are co-planar, in the 'zero' plane, at the zero angle of θ and 2θ (to ± 5 μm and $\pm 0.001^\circ$); and
(5) the incident beam is centred on both the equatorial and 'zero' planes (to $\pm 0.05^\circ$).

The first three conditions are established with the X-rays off, while conditions (4) and (5) are achieved with the beam present, as it is actively used in the alignment procedure. Neither incident- nor diffracted-beam monochromators are considered; they are simply added on to the Bragg–Brentano arrangement and have no effect on the issues outlined here. Also, in order to execute this procedure, a sample stage that can be rotated by 180° in θ is required. However, this does not need to be the sample stage used for data collection. Before any concerted effort to achieve proper alignment, it is advisable to check the mechanical integrity of the equipment. Firmly but gently grasp a given component of the diffractometer, such as the tube shield, receiving-slit assembly or sample stage, and try to move it in a manner inconsistent with